ELECTROABSORPTION

The absorption of radiation is one of the most widely occuring physical processes in nature. Colors of liquids and solids are determined by how they absorb light. Absorption processes are also used to convert light energy into other energy forms, such as electrical energy in solar cells, chemical energy in the photosynthesis of plants, and other light energies in some lasers. Absorption is utilized in countless household items: everything from televisions and photographic film to water heaters and microwave ovens.

Electroabsorption refers to the absorption of light or heat energy by some material in the presence of an electric field. One quality of electroabsorption is that the amount of absorption depends on the strength of the electric field. Historically, absorption measurements have been used as a tool to study the electrical and optical properties of various materials. By varying (modulating) the electric field while performing these absorption measurements, much more insight has been gained about the structure of matter (1). Electroabsorption measurements have helped to reveal the structures of very complicated materials, particularly semiconductors. The field of study of electroabsorption is immense, spanning a sizable portion of physics and engineering research over the past forty years. Out of this work has come a good understanding of the interaction between radiation and matter in the presence of an electric field.

In parallel with the study of electroabsorption, there has been a paradigm shift, in recent years, to use semiconductor materials to build better systems, accompanied by the need for faster, lower-cost, and higher-reliability components. In addition to larger scales of production, more functionality is being achieved by the basic device. The capabilities of monolithic integration as well as integration with dissimilar materials (2) makes the use of semiconductor devices the serious choice for use in all varieties of electronic systems. Beside the high-speed electronic signal processing for which semiconductors are well known, there have been myriad investigations into the use of semiconductor materials for optoelectronics. One common example of semiconductor optoelectronics is a semiconductor diode laser. A number of semiconductor materials are capable of converting electric signals into optical signals, and vice versa, with estimated time constants as low as 50 fs (3). The research has come full circle on semiconductors, and the method of electroabsorption modulation is being revisited as a key tool in optoelectronics.

OPTICAL COMMUNICATION

Optoelectronic systems are used routinely in telecommunication, satellite communication, and computer networking. Most high-speed or high-capacity information systems stand to benefit from the use of optical transmitters and receivers because of the tremendous increase in bandwidth that the technology supports. For example, the increased usage of home computers and the Internet is a major driving force to provide more bandwidth than previously thought achievable through telephone line. As the demand for bandwidth grows, the optoelectronic components are expected to get closer and closer to individual end-users. Other occurances of optical transmission are found in signal distribution, information processing, and remoting sensing.

An optical communication system that uses a fiber optic cable (referred to as a link) is sometimes a more cost-effective solution in medium- to long-haul transmission. Optical fiber possesses a small attenuation loss (0.2 dB/km to 0.4 dB/km), can handle large subcarrier frequencies without the need to develop high-frequency electronic signal repeaters, and is immune to electromagnetic interference. For these reasons, optical communication is a very promising technology.

For effective use of optical communication in antenna remoting or signal distribution, some key technological concerns must be addressed. Of fundamental importance for the link are the RF efficiency, noise figure, linear dynamic range, and speed of operation or bandwidth; also considered important are the compactness of the system (including all supporting components), and the polarization and temperature sensitivity. These link requirements subsequently place requirements on all of the components that comprise the link. These include the transmitter, which consists of the optical source and the electrical-to-optical mixer (modulator), the transmission fiber, and the optical detector (receiver), which is the optical-to-electrical down-converter. Presently, high power (several hundred mW), low noise (less than -165 dBc/Hz) optical sources are available commercially, as are high quality, low-loss optical fiber. Of the other two components, the modulator and the detector, the modulator has the strictest requirements in terms of linearity, noise figure, frequency response, optical loss, and polarization sensitivity.

Comparison of Technologies

For intensity modulation and direct detection of the optical carrier, either direct modulation or external modulation may be used in the transmitter. In direct modulation, a laser diode acts as both light source and modulator. In external modulation, the laser and modulator are separate units, typically with light coupled from the laser via a fiber to a waveguide modulator. It is also possible to integrate the laser and modulator on the same chip. External modulation is typically used for link applications from the ultra-high frequency (UHF) band to millimeter wavelengths that have the largest demands on dynamic range and lowest noise figure. Direct modulation has several advantages in terms of compactness and simplicity, as there is need for only one device instead of two in the transmitter, the semiconductor lasers used are small, and there is only one fiber to couple. However, there is a major drawback for long-distance, high-speed data links. The effect of wavelength chirp (change in refractive index) in lasers under direct modulation (4) limits the distance-frequency product over which the directly modulated link can transmit information, before dispersion in the fiber significantly distorts the signal. It is possible to extend the transmission range of a chirped signal by dispersion management in the fiber (5). External modulation also may induce wavelength chirp, but the chirp of external modulation can be much smaller than for direct modulation.

Optical communication systems can use either analog or digital information formats, as system requirements differ from application to application. In analog RF systems, chirp considerations tend to favor external modulation for maximizing the linear dynamic range of high-speed fiber optic links. Linearity is a basic issue for analog transmission that cannot be circumvented by simply converting the analog signal to a digital signal (A/D) at the front-end of the link. In the most demanding analog applications at microwave frequencies, pushing the problem off to A/D conversion would degrade the fidelity of the link by introducing quantization errors.

Mach–Zehnder Modulators. Guided-wave external optical modulators are important optoelectronic devices for the transmission of microwave signals over optical fibers. Electrorefractive devices have been the mainstay of integrated optical modulators for many years. Such devices operate through a voltage-controlled variation of the optical phase. While the present discussion is not intended to be exhaustive on the many configurations of electrorefractive optical modulators, a description of a basic modulator device is presented for comparison to the semiconductor modulator. Attention is given to system performance with an emphasis on size, speed, and drive voltage.

Lithium niobate ($LiNbO_3$) is a commonly used material for either pure phase modulators or amplitude modulators (in either a Mach–Zehnder interferometer arrangement or as a switched directional coupler). The basic Mach–Zehnder modulator (MZM), for example, consists of an optical waveguide that splits the light equally into two paths that recombine after some interaction length. A voltage applied to one of the optical paths creates a differential optical phase proportional to the product of the voltage and length (6). The recombined output produces coherent interference in the two optical fields, therefore modulating the intensity with a cosine-squared dependence in the applied voltage. It is common to put electrodes over both paths in a push–pull arrangement ($+V$ to first electrode and $-V$ to second electrode), so that the modulation efficiency, which is proportional to the inverse of the applied voltage, is improved by a factor of two for a given length. The modulation dependence on the voltage-length product represents a tradeoff between sensitivity and bandwidth. In order to achieve full modulation for a 5 V driving signal, the interaction length must on the order of 1 cm. To reduce the driving voltage, a longer device is required, which increases the device capacitance for a lumped-element modulator.

The speed of operation of a lumped-element electrode modulator, as described above, is limited by the charging capacitance of the electrodes. The applicable figure of merit for waveguide modulators is the bandwidth to drive the voltage ratio (B/V), which is defined by the 3 dB electrical frequency response into a matched load (a 50 Ω resistor for a 50 Ω system) and the voltage required to give a π phase shift, V_π (6). The largest B/V ratio that is expected for an optimized modulator with lumped-element electrodes is approximately 0.67 GHz/V at 1.32 μm optical wavelength.

To overcome the speed limitation of charging capacitance, traveling-wave electrode devices have been used. The traveling-wave electrode is intended to be an extension of the transmission line that delivers the signal to the optical modulator, thus requiring the same characteristic impedance. A structure in which the RF traveling-wave velocity equals the optical waveguide propagation velocity can improve the modulation bandwidth, with the maximum speed limited only by microwave attenuation due to the finite conductivity of the electrode. One of the best reported velocity-matched, impedance-matched Mach–Zehnder interferometers has a 39 GHz 3 dB electrical bandwidth and a V_π of 5.0 V at 1.5 μm, giving a B/V ratio of 7.8 GHz/V (7).

Semiconductor Electroabsorption Waveguide Modulators. In contrast to the electrorefractive class of modulators discussed above, electroabsorption (EA) modulators operate through a voltage-controlled change in light absorption. EA waveguide devices have been studied primarily for use in high-bit-rate digital transmission due to their low drive voltages and com-

patibility with high-speed electronic driver circuits. These two features are also attractive for many analog RF systems, and as such, EA modulators deserve close attention for use in analog RF systems. This section reviews the state-of-the-art for semiconductor EA modulators, pointing to some of the advantages for using such devices for analog transmission.

Semiconductor-based modulators have some clear advantages over modulators based on other materials. First, the semiconductor modulators are small, which allows for packaging the devices at a higher density than, for example, $LiNbO_3$ based devices. The smaller size also permits the modulator electrodes to be treated as a lumped-element capacitance at microwave frequencies, which significantly simplifies the subsequent microwave design. Second, the semiconductor modulators are based on III–V semiconductor technology. Due to the mature processing technology of III–V semiconductors, modulators can be monolithically integrated in photonic integrated circuits, with DFB laser sources, and with their microwave driver circuits. Subsequently, semiconductor EA modulators are more suitable for array integration.

Most semiconductor EA modulators operate through either the Franz–Keldysh effect (FKE) (8,9) in bulk semiconductor layers, or the quantum-confined Stark effect (QCSE) (10) in multiple quantum well (MQW) layers. Waveguide devices have been made with optical insertion losses less than 5 dB for both types of modulator.

Figure 1 shows the band diagrams under an applied electric field for a bulk absorbing layer and a quantum well, which illustrate the subtle difference between these two EA effects. For the bulk layer, an electron in the valence band is able to make a transition to the conduction band by absorbing the energy from a photon. Without the electric field, this transition will only take place for photon energies greater than, or equal to, the bandgap energy. In the presence of the electric field, the transition can occur with a photon energy less than the bandgap energy by the Franz–Keldysh effect. The tilting of the bands by the electric field creates a triangular barrier for the excited electron to tunnel through to the conduction band. One can consider this transition process a photon-assisted interband tunneling. As the electron vacates the valence band, it is considered to leave a hole state in its place. This process also involves a phonon in indirect bandgap transitions. For direct bandgap transitions, the electron moves in a preferred direction to conserve momentum. In the quantum well structure, a small bandgap (well) material is sandwiched between larger bandgap (barrier) material. Figure 1 illustrates a symmetric quantum well, having the same barrier material on both sides. The quantum confinement (typically on the order of 300 Å or less) causes quantization of the allowed energy levels, as in the one-dimensional particle in a box (11). These energy levels occur intermediate to the independent band edges of the two materials. Another consequence of the quantum confinement is a strong Coulombic interaction between electrons and holes in the well, which produces an excitonic state (12). The result of the exciton is an enhancement in the absorption strength below the allowed-state transition energy at room temperatures (10).

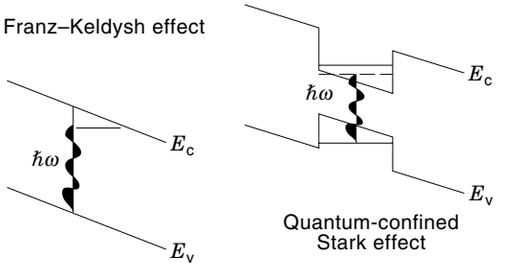

Figure 1. Energy band diagrams under an applied electric field show the subtle difference between the Franz–Keldysh effect in a bulk absorbing layer and the quantum-confined Stark effect in a quantum well. Light of energy $h\nu$ is absorbed in the bulk material if an electron can tunnel through the triangular barrier to the conduction band. In the quantum well, light is absorbed to a Coulombic state lower in energy than the allowed transition energy defined by the confined quantum states.

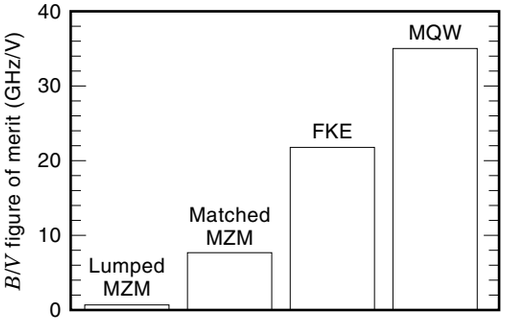

Figure 2. Reported B/V figures of merit for the lumped Mach–Zehnder, matched Mach–Zehnder, FKE, and MQW modulators. For a specific operating frequency, the electroabsorption modulators require a smaller drive voltage than the Mach–Zehnder modulators.

The MQW modulators offer some advantages in terms of the ability to be optimized for specific device performance. Most notably, MQW modulators have simultaneously achieved high-speed and low-drive voltage. The B/V figure of merit, used earlier for the MZM, is defined by the 3 dB electrical frequency response and the voltage required to extinguish the optical power by 10 dB for EA modulators. This modified definition is used since the EA modulator does not have a periodic transfer curve like the MZM. EA modulators with 3 dB frequencies of 40 GHz to 50 GHz have been reported with B/V values of 17 GHz to 18 GHz/V (13). The best reported value of B/V for an MQW device is 35 GHz/V (14). FKE devices typically yield a more modest B/V ratio, due to a smaller change in absorption per waveguide length compared to MQW devices. The best value reported for a FKE modulator is 20 GHz/V (15). These values are shown in Fig. 2 along with those of the MZM. It is interesting to note from the B/V figure of merit, that lumped-element EA modulators perform better than the best velocity-matched, impedance-matched MZM. Thus, for a specific operating frequency, the EA device possesses better modulation efficiency than the Mach–Zehnder, which translates into better link gain, noise figure, and linear dynamic range.

One deficiency of electroabsorption modulators, compared to MZMs, is power handling ability. This is influenced by two factors. First, the more compact size of the electroabsorption active area translates into a larger optical intensity than for a MZM at equal optical power. Second, the electroabsorption device generates carriers that do not move out of the active

area fast enough at large intensities. Carrier trapping can limit the utility of the device as saturation starts to occur (16). Recently, work has been done to improve the power handling properties of MQW modulators with strained materials (17).

More care is necessary when comparing the FKE with the QCSE. While MQW waveguide modulators have achieved remarkable performance for a few criteria, they often suffer in either one or more other performance areas. Due to the material structure of MQW modulators, they generally possess a larger temperature sensitivity than FKE modulators. In order to achieve many of the desired features simultaneously in a MQW, very intricate growth procedures or complex device design is required. Recently, a high-speed, high-saturation power, and polarization-insensitive MQW device has been demonstrated (18). Such a device would be an excellent candidate for use in analog systems. Generally, better contrast ratios are obtainable with MQW devices, which make them preferred over FKE devices for digital transmission. On the other hand, double-heterojunction modulators, based on the Franz–Keldysh effect, are very simple to fabricate and manufacture, due to the accumulated experience of laser and detector technologies in related materials. Additionally, FKE devices possess smaller inherent polarization anisotropy. For these reasons, it is not clear which electroabsorption mechanism is better for use in high-performance analog fiber-optic links.

MODELING THE ELECTROABSORPTION MODULATION TRANSFER CURVE

The remainder of this article will focus on modeling the modulation transfer curve of the electroabsorption device. Whether the light is transmitted through an optical fiber or free space, the modulation transfer curve specifies the relation between the input electronic signal and the output optical signal. The necessary models for analyzing both surface-normal and waveguide electroabsorption modulators are developed from the pertinant electroabsorption theory for bulk and quantum well semiconductors. From an understanding of the electroabsorption mechanisms, simple device transfer curves are derived. These models are then compared to real device measurements for verification.

Electroabsorption Theory

The following sections contains a review of the theory used to derive expressions for the absorption strength of bulk and quantum well materials. Closed-form solutions for computation are desired wherever possible, but accuracy is also desired. The theory primarily relies upon results from quantum electrodynamics, band theory, and other areas of solid-state physics where applicable. The standard approach is to apply time-dependent perturbation theory to solve for the transition probabilities that determine the absorption cross section. The calculations use the effective mass approximation of Dresselhaus (19) and the electric dipole approximation, in which the bands are assumed parabolic, the momentum matrix elements are independent of the wave vector, and the interband reduced masses are nearly constant (20). These approximations are appropriate for one-electron solutions and for Wannier (weakly bound) excitons (12) in direct bandgap transitions. The field-dependence of the electron and hole wavefunctions and eigenenergies are given and discussed for the FKE and the QCSE. The polarization dependence of the incident optical radiation is also dealt with in the calculation of the absorption strength. Finally, the assumptions used in the calculations are discussed.

The Dielectric Function. The complex dielectric function

$$\epsilon = \epsilon_1 + j\epsilon_2 = \epsilon_0(\epsilon' + j\epsilon'') \tag{1}$$

determines the propagation of electromagnetic waves through matter, where ϵ_1 and ϵ_2 are the real and imaginary parts of the dielectric function, ϵ' and ϵ'' are relative dielectric constants, and ϵ_0 is the dielectric constant in vacuum. The absorption cross section is defined with respect to the quantity ϵ_2 according to

$$\alpha\epsilon_0 = \frac{\omega\epsilon_2(\omega)}{nc} \tag{2}$$

where ω is the radiation frequency in rad/s, c is the speed of light in vacuum, and α is the absorption coefficient. The index of refraction, n, and the index of absorption, κ, are the real and imaginary parts, respectively, of the square root of Eq. (1).

$$\sqrt{\frac{\epsilon}{\epsilon_0}} = n + j\kappa = n + j\frac{c\alpha}{2\omega} \tag{3}$$

The index n is known to factor into the speed of the wave propagating through the material,

$$v = \frac{c}{n} \tag{4}$$

as well as determine angles of refraction at interfaces. In EA modulation, both n and κ change with the applied field, F. Thus the change in ϵ with field is written

$$\Delta\epsilon(\omega, F) = \epsilon(\omega, F) - \epsilon(\omega, 0) = \Delta\epsilon_1(\omega, F) + j\Delta\epsilon_2(\omega, F) \tag{5}$$

The corresponding change in α with field is (21)

$$\Delta\alpha(\omega, F) = \frac{-\omega\kappa}{c(n^2+\kappa^2)}\Delta\epsilon_1(\omega, F) + \frac{n\omega}{c(n^2+\kappa^2)}\Delta\epsilon_2(\omega, F) \tag{6}$$

Near the fundamental band edge, $\kappa \sim 0$, so that $\Delta\alpha \propto \Delta\epsilon_2$. However, if κ becomes as large as 10% of n, $\Delta\epsilon_1(\omega, F)$ can be calculated approximately from $\Delta\epsilon_2(\omega, F)$, provided that $\Delta\epsilon_2$ is nonzero over a small range of ω. By the Kramers–Krönig relation (21)

$$\Delta\epsilon_1(\omega) \cong \frac{1}{\pi\omega^2}\mathrm{PV}\left[\int_{-\infty}^{\infty}\frac{d\omega'}{\omega'-\omega}\omega'^2\Delta\epsilon_2(\omega')\right] \tag{7}$$

where PV represents the principal value of the integral.

Fermi's golden rule is used to calculate the absorption coefficient for an electron transition. The fundamental result (22)

$$\alpha = \frac{4\pi^2e^2}{\epsilon_0 nc\omega m_0^2 V}\sum_{s,\,\Delta k}|\hat{\epsilon}\cdot\langle\varphi_f|\boldsymbol{p}|\varphi_i\rangle|^2\,\delta(E_f - E_i - \hbar\omega) \tag{8}$$

states that the absorption coefficient is a summation over spin states and possible electron wave vectors in the first Brillouin

zone (the first reciprocal-lattice space), with the difference between the initial and final electron energies (E_i and E_f) equal to the absorbed photon energy $\hbar\omega$. The absorption strength depends on the projection of the electromagnetic-wave polarization vector on the electron momentum vector, as it makes its transition from the initial (ground) state to the final (excited) state.

The theory is extended to crystals by inclusion of band theory. Semiconductor crystals are well described by band theory, in which the valence band is almost full with electrons, and the conduction band is practically empty of electrons. Current flow occurs when a hole (missing electron) in the valence band moves in the opposite direction as an electron in the conduction band. The two particles have different effective masses in each band. It seems that the involvement of an electron and a hole in the absorption of a photon would require a solution to a two-particle Schrödinger equation. However, the effective mass approximation allows for the expression of the electron-hole pair in terms of single particle states, with an envelope function to describe the pair correlation (19). Elliot first used this theory to solve for the excitonic state produced through the Coulomb interaction potential, $e^2/\epsilon r$, of the generated electron and hole pair subsequent to photon absorption (23). Elliot considered the case of weak binding of the electron-hole pair, but his result is valid for any simple potential that yields a closed-form solution for the envelope function.

Incorporating Elliot's result, the absorption coefficient of Eq. (8) becomes

$$\alpha = \frac{4\pi^2 e^2}{\epsilon_0 nc\omega m_0^2 V} \sum_{\boldsymbol{s},\,\Delta\boldsymbol{k}} |\hat{\epsilon}\cdot\langle\varphi_C|\boldsymbol{p}|\varphi_V\rangle|^2 |\Phi_{CV}(0)|^2 \delta(E_C^0 - E_V^0 - \hbar\omega) \tag{9}$$

where $\Phi_{CV}(r)$ is the envelope wavefunction, and the subscripts C and V refer to Bloch states (periodic in the crystal) in the conduction and valence bands, respectively. The significance of this result is that the absorption strength can be calculated from any envelope wavefunction which satisfies an effective-mass Schrödinger equation.

Electric Field Dependence. With Eq. (9) as a tool, the electric field dependence of the absorption can be evaluated. It should be mentioned, however, that simple closed-form solutions do not exist if the static potential in the Hamiltonian is a combination of the Coulomb field and a linear electric field (1).

Early work in the EA theory for bulk materials neglects the Coulombic interaction potential altogether. Tharmalingam (24) solved the exact electric-field dependence for the FKE, using Elliot's result for zero-field excitons to determine the absorption solely in the presence of a linear electric field. This is seemingly justified by the weak field that is necessary to ionize the exciton at room temperature. The result shows both an exponential-type tail below the bandgap and oscillatory behavior above the bandgap. To include the Coulombic interaction, numerical approaches are necessary. Their main result is very good agreement to low-temperature measurements.

For quantum well structures, however, the Coulombic interaction is very important at room temperature, because the carriers are confined within the Bohr radius, inhibiting field ionization of the exciton (25). Fortunately, in describing the QCSE within the EMA, it has been shown through numerous variational and fully numeric calculations that the electric field primarily perturbs the electron and hole confinement energies with a second-order Stark shift, and has a small impact upon the exciton binding energy. In these quasi-two-dimensional analyses, a small shift in the exciton binding energy with electric field is predicted, although the shift saturates somewhat at large electric fields, as the individual particles are pulled to the opposite sides of the well (25). Whether 2-D or quasi-2-D excitonic theory is used, the quantum well oscillator strength only depends upon the overlap in the field-dependent single-particle envelope wavefunctions.

The 3-D Franz–Keldysh Effect. The reader is referred to (26) for a derivation of the Franz–Keldysh effect from Eq. (9). The absorption coefficient for the Franz–Keldysh effect is given by

$$\begin{aligned}\alpha_{FKE} = {} & \frac{2\pi e^2}{\hbar\omega\epsilon_0 ncm_0^2} |\hat{\epsilon}\cdot\langle\varphi_C|\boldsymbol{p}|\varphi_V\rangle|^2 \left(\frac{2\mu}{\hbar}\right)^{3/2} \\ & \times \left\{ \frac{\omega-\omega_g}{\sqrt{\omega_F}} |Ai(\beta)|^2 + \sqrt{\omega_F}\,|Ai'(\beta)|^2 \right\}\end{aligned} \tag{10}$$

where $\beta = (\omega_g - \omega)/\omega_F$, $\hbar\omega$ is the photon energy, $\hbar\omega_g$ is the bandgap energy, and $\hbar\omega_F$ is the field-induced electrooptic energy defined by

$$\omega_F = \left(\frac{e^2 F}{2\mu\hbar}\right)^{1/3} \tag{11}$$

The difference $\hbar\omega_g - \hbar\omega$ is commonly referred to as the detuning energy, E_{det}. It is observed that both terms in the braces of Eq. (10) depend on the electric-field and the detuning energy, through the factors ω_F and β. Therefore, the electric field and detuning energy represent two material-independent controls of the absorption coefficient.

It is observed from dimensional analysis of Eq. (10) that the absorption coefficient has units of cm^{-1}. Therefore, the total absorbed power for bulk materials depends on the interaction length, L, according to

$$A = P_{\text{opt}}(1-R)[1 - e^{\alpha(F_z)L}] \tag{12}$$

where P_{opt} is the incident optical power, and R is the Fresnel reflectance from the air to the semiconductor. This exponential form is the basis for the voltage-controlled absorption of the bulk EA material.

Quantum-Confined Stark Effect. The electric-field dependence and the optical absorption strength for the QCSE in quantum well materials is given in (27). In addition to the typical quantization of certain parameters, such as allowed energies and momentum, the confinement in the quantum wells lowers the spatial dimension of the system, permitting 2-D analysis. The QCSE accurately describes the absorption coefficient of quantum well semiconductor materials that have relatively thick barriers, approximately the size of the excitonic Bohr radius.

For the symmetric quantum well of Fig. 1, there are three potentials of interest. First, there is the potential from the externally applied bias, which is assumed to produce a con-

stant electric field across the well and barriers. Second, there is the confinement potential, due to the bandgap discontinuity between the well and barrier material; these are modeled as step-discontinuities. Last, there is the Coulomb interaction potential between the photogenerated electron and hole that produce the excitonic effects. The resulting 2-D absorption coefficient is

$$\alpha^{2D}(\omega) = \frac{4\pi^2 e^2}{\epsilon_0 n c \omega m_0^2} |\hat{\epsilon} \cdot \langle \varphi_C | \boldsymbol{p} | \varphi_V \rangle|^2 \cdot |\langle f_c | f_v \rangle|^2 \cdot \frac{1}{\pi a_B^2} \times \left\{ \sum_{l_q} \frac{1}{(l_q + \frac{1}{2})^3} \delta(\hbar\omega - E_g^{2D} - E_b^{l_q}) + \frac{\Theta(\hbar\omega - E_g^{2D})}{R_y \left[1 + e^{-2\pi \sqrt{R_y/(\hbar\omega - E_g^{2D})}} \right]} \right\} \tag{13}$$

where f_c and f_v are the electron and hole envelope-functions perpendicular to the layers, a_B is the exciton Bohr radius, R_y is the Rydberg energy, E_g^{2D} is the allowed transition energy, l_q represents the principle quantum number, E_b is the exciton binding energy, and $\Theta(x)$ is the unit step function. Equation (13) includes contributions to the absorption by excitons and the allowed direct transitions. The summation of delta functions are the exciton resonances that occur at photon energies E_b below the allowed transition energies. The term with the unit step function corresponds to the allowed transitions for unbound excitons. The factor $\langle f_c | f_v \rangle$ is the overlap integral of the z-component single-particle envelope wavefunctions. Numerical calculation is used to solve for both E_g^{2D} and $\langle f_c | f_v \rangle$ as a function of the electric field. For a finite-depth well, a finite number of bound state (confinement) energies exist. The energies for the electron, $E_{e^q}^{n_q}(F)$, and hole, $E_{h^q}^{n_q}(F)$, are determined (27) from the transcendental equation

$$\sqrt{\frac{E_{e,h}^{n_q}}{E_1^\infty}} \cot^2 \left(\frac{\pi}{2} \sqrt{\frac{E_{e,h}^{n_q}}{E_1^\infty}} \right) = \frac{m_w}{m_b} \sqrt{\frac{V_{e,h} \pm eFz_{e,h} - E_{e,h}^{n_q}}{E_1^\infty}} \tag{14}$$

where m_w and m_b are the well and barrier effective masses, n_q is the principle quantum number for the 1-D particle in a box, and E_1^∞ is the infinite well ground state energy,

$$E_1^\infty = \frac{\hbar^2}{2m_{e,h}} \left(\frac{\pi}{L_z} \right)^2 \tag{15}$$

For bound states, the electron and hole envelope wavefunctions are field-shifted sinusoids in the well and decay exponentially into the barriers. The unbound wavefunctions are plane waves. As there is no closed form solution for Eq. (14), there are no exact expressions for the bound wavefunctions. The electron and hole allowed energy levels and wavefunction overlap in the z-direction are determined by means of a three-point finite difference method calculation for a constant electric field across the well and barrier. The numerical calculation constructs the normalized wavefunctions, the normalized wavefunction overlap integral, and values of the transition energies (E_g^{2D}) for several modes of light hole-to-electron and heavy hole-to-electron transitions. The electric field is varied, and the absorption coefficient spectrum is calculated at a number of specified detuning energies.

The discrete 2-D transition energies are calculated from the electron and hole eigenvalues, equivalent to the solutions of Eq. (14), according to

$$E_g^{2D}(F_z) = E_g^{(w)} + E_e(F_z) + E_h(F_z) \tag{16}$$

where $E_g^{(w)}$ is the bandgap energy of the well material. The normalized overlap integral is

$$\langle f_c | f_v \rangle = \frac{1}{\sqrt{N_c^{1D} N_v^{1D}}} \sum_{z_i} f_c(z_i) f_v(z_i)\, dz_i \tag{17}$$

where dz_i is the distance between mesh points, and N_c^{1D} and N_v^{1D} are the normalization factors for each wavefunction.

Exciton broadening is determined from the probability that the electron tunnels out of the well each time it hits the barrier wall. The position at which the electron effectively tunnels out of the well is the distance at which the barrier potential is lowered to the energy of the confined state,

$$z_B = \frac{\Delta E_C - E_e}{eF} \tag{18}$$

The tunneling probability is given by

$$P_t = \frac{1}{\gamma_c N_c} \sum_{z_i} |f_c(z_i)|^2\, dz_i \tag{19}$$

where

$$\gamma_c = \frac{\sum_{z_i \in \text{well}} |f_c(z_i)|^2\, dz_i}{\sum_{z_i} |f_c(z_i)|^2\, dz_i} \tag{20}$$

is the confinement of the electron within the well, and the integrand at z_B is interpolated from the cubic spline of discrete wavefunction values on either side of z_B.

The exciton broadening is assumed to be Gaussian, with an energy linewidth for the 1S state given by the expression

$$\Gamma_{\text{exc}} = \frac{\pi P_t}{8 m_{e(w)}^*} \left(\frac{\hbar}{L_z} \right)^2 \tag{21}$$

Additionally, a broadening function with a phenomenological full-width-at-half-maximum (FWHM) is introduced to better model the real situation of thermal and inhomogeneous linewidth broadening of the zero-bias exciton line. The resulting absorption coefficient for the 1S exciton with Gaussian broad-

ening becomes

$$\alpha_{QCSE}(\omega) = \frac{4\pi^2 e^2}{\epsilon_0 nc\omega m_0^2} |\hat{\epsilon} \cdot \langle \varphi_C | \boldsymbol{p} | \varphi_V \rangle|^2 \cdot |\langle f_c | f_v \rangle|^2 \cdot \frac{1}{\pi a_B^2} \cdot \{e^{-(\hbar\omega)^2 \langle f_c | f_v \rangle / \mathrm{FWHM}}\} \otimes \left\{ 8\delta(\hbar\omega - E_g^{2D}(F_z) - E_b^0) \otimes e^{-(\hbar\omega)^2/\Gamma_{\mathrm{exc}}} + \frac{\Theta(\hbar\omega - E_g^{2D}(F_z))}{R_y \left[1 + e^{-2\pi\sqrt{R_y/(\hbar\omega - E_g^{2D}(F_z))}}\right]} \right\} \tag{22}$$

where $\otimes$ denotes the convolution integral, FWHM refers to the zero-bias exciton Gaussian linewidth, and Γ_{exc} is a field-induced broadening parameter.

Dimensional analysis of Eq. (22) shows that the 2-D absorption coefficient is unitless. Thus, Eq. (22) is interpreted as the effective absorption coefficient per well. It is more convenient, however, to deal with an absorption coefficient that has units of cm^{-1} like the 3-D FKE absorption coefficient for compatibility with Eq. (12). When a photon is absorbed, the photogenerated electron and hole are confined in the z-direction until the carriers tunnel out of the well. Therefore, it is customary to divide α^{2D} by the well width, L_z, resulting in an absorption coefficient with units of cm^{-1}.

Polarization Dependence and Calculation of the Matrix Elements. The calculated absorption coefficients have assumed nothing yet about the state of polarization. In the treatment of the optical absorption as an electric dipole transition, however, one has inherently assumed some quantum mechanical selection rules. In fact, these selection rules are those for transitions of the electric dipole. In this discussion, the transition matrix element will be written $\langle j' m_q' | \boldsymbol{p}_q | j m_q \rangle$, where j is the quantum number of the total angular momentum, m_q is the magnetic spin quantum number corresponding to the operator J_z, which is the z-component of the total angular momentum operator, and q is the rotational quantum number of the operator. The values with primes denote the final state, and those without denote the initial state.

The band structure of the semiconductor consists of two pairs of upper valence bands and a pair of lower conduction bands, with each pair containing two spin orientations. The upper valence bands have a total angular momentum $j = 3/2$, and for the bulk semiconductor, these are degenerate at the zone center. The bands are distinguished by their magnetic quantum number: bands with $m_q = \pm 3/2$ are the heavy hole bands, and the bands with $m_q = \pm 1/2$ are the light hole bands, so named because the effective masses in the Luttinger–Kohn Hamiltonian (28) are different. The lowest conduction bands have a total angular momentum of $j' = 1/2$. Therefore, the magnetic quantum number may only assume the values of $m_q' = \pm 1/2$.

From purely kinematic and geometric considerations, the dipole matrix element vanishes unless the *m-selection rule* is satisfied, namely,

$$m_q' = q + m_q \tag{23}$$

For the electric dipole transition, if $\boldsymbol{p} \| \hat{z}$, then $q = 0$. If $\boldsymbol{p} \perp \hat{z}$, then $q = \pm 1$. It is evident from these relations and from the selection rule, that $m_q = \pm 3/2$ transitions are not allowed for $q = 0$. The ratio of the dipole projections onto each principal crystallographic direction are thus

$$|P_z^{(hh)}|^2 : |P_x^{(hh)}|^2 : |P_y^{(hh)}|^2 = 0 : \tfrac{3}{4} : \tfrac{3}{4} \tag{24}$$

$$|P_z^{(lh)}|^2 : |P_x^{(lh)}|^2 : |P_y^{(lh)}|^2 = 1 : \tfrac{1}{4} : \tfrac{1}{4} \tag{25}$$

In the bulk material, the light- and heavy-hole subbands are degenerate at zone center. Therefore, the total absorption coefficient for a given polarization is the sum of the contributions of the heavy hole and light hole transitions, multiplied by the appropriate polarization prefactors. For light polarized perpendicular to the dielectric layers (TM polarization), the relative strengths of heavy- and light-hole transitions are 0 and 1, respectively. For light polarized parallel to the layers (TE polarization), the relative strengths of heavy- and light-hole transitions are 3/4 and 1/4 . Therefore, the total absorption coefficient for each polarization state is obtained by adding the heavy and light hole components.

$$\alpha_{\mathrm{TE}} = \tfrac{1}{4}\alpha_{\mathrm{LH}} + \tfrac{3}{4}\alpha_{HH} \tag{26}$$

$$\alpha_{\mathrm{TM}} = \alpha_{\mathrm{LH}} \tag{27}$$

For the unstrained quantum well, it is noted that the confinement lifts the degeneracy of the valence bands, so the heavy hole and light hole transitions occur at different energies (10). The strength of the transitions for each hole subband are still modified by the same polarization prefactors. However, the electron-to-heavy hole exciton is of larger interest, since it occurs at a lower energy than the electron-to-light hole exciton. Subsequently, the quantum well structures have an extreme polarization anisotropy between TE and TM polarizations. Due to this anisotropy, quantum well modulators are typically operated in the TE polarization.

The matrix elements in Eqs. (10) and (22) are now computed. Reference (29) has tabulated these matrix elements for various binary III–V zinc-blende materials in terms of an associated energy,

$$E_P = \frac{2}{m_0} |\langle \varphi_C | \boldsymbol{p} | \varphi_V \rangle|^2 \tag{28}$$

The electric dipole projection along any one of the principle crystallographic axes is assumed to be 1/3 (30), so

$$\frac{2}{m_0} |\hat{e} \cdot \langle \varphi_C | \boldsymbol{p} | \varphi_V \rangle|^2 = \tfrac{1}{3} E_P \tag{29}$$

Vegard's law, which allows stoichiometric interpolation of energies, is used to determine the value of E_P for different materials. In the $In_{1-x}Ga_xAs_yP_{1-y}$ system,

$$E_P = (1-y)E_P^{\mathrm{InP}} + xE_P^{\mathrm{GaAs}} + (y-x)E_P^{\mathrm{InAs}} \tag{30}$$

Furthermore, if the alloy is lattice-matched to the InP substrate, the relation

$$x = 0.468y \tag{31}$$

Table 1. Material Bandgap Energies, Transition Matrix Element Energies, and Indices of Refraction

Material	Bandgap Energy	E_P	Wavelength	Index of Refraction
InGaAs	0.751 eV	23.4 eV	1.5435 μm	3.592
InGaAsP	1.0063 eV	22.2 eV	1.318 μm	3.458
InP	1.351 eV	20.4 eV	1.5435 μm	3.168

must hold. The transition matrix element associated energies for the different lattice-matched materials used to verify the electroabsorption models are tabulated in Table 1.

Assumptions and Nonidealities. This section highlights the few assumptions that are made in modeling the absorption coefficients for the QCSE and the FKE, and points to the expected limitations from those assumptions. The electric field has been assumed constant throughout the active layer. For the absorption coefficient derivations, the electric field is assumed constant in order to give tractable solutions to the Schrödinger equations. In a real device, such as a p–i–n structure, the electric field is not truly constant, but rather a linear function of the distance from the p–i junction (as the intrinsic region is lightly doped n-type). Depending on the background doping level or the carrier density in the intrinsic layer, the assumption of a constant electric field may not be justified. For an intrinsic layer doping concentration at least two orders of magnitude smaller than the p-layer doping concentration, the assumption of a constant electric field is acceptable. However, for large illumination intensities, the photogenerated carrier densities may screen the electric field and result in a drastically nonuniform electric field in the active layer (31).

If the electric field becomes severely nonuniform because of saturation, or if generally more accuracy over the constant field case is desired, finite element analysis (FEA) may be required to obtain better accuracy for the absorption characteristics. The benefit of FEA is that the electric field is assumed constant over a small finite element of absorption, in which case the constant-field absorption model may be applied. Such a simulation needs to incorporate the Poisson and carrier continuity equations to solve for the electric field distribution. The total absorption is summed over all the finite elements. This approach is applicable to the FKE absorption coefficient. However, for modeling the QCSE, a FEA needs to simultaneously solve the carrier transport equations and the 1-D Schrödinger equation, because the nonuniform electric field alters the quantum potential, giving solutions different from those of Eq. (14).

Another practical concern is that the EA devices are controlled by an applied bias voltage, and at zero applied bias, the electric field is nonzero, due to the diode junction built-in voltage, V_{bi}. Due to the assumption of a constant electric field, the electric field is simply modeled

$$F = \frac{V_{\text{bi}} + V}{d} \tag{32}$$

where V is the applied voltage, and d is the intrinsic layer thickness.

Note that with this formulation, it is possible to estimate the residual material absorption loss, that is $\alpha(V = 0)$ due to the electroabsorption effect. However, this is the only loss that is modeled. Both interconduction band and free-carrier absorption have been neglected. These absorption mechanisms are directly proportional to current density (32), and therefore depend on the electric field by strict consideration. However, at photon energies below the bandgap, these values are approximately less than 1 cm^{-1} at 10^{17} cm^{-3} carrier concentrations for both GaAs and InP. In the intrinsic region, carrier concentrations are not expected to reach such large levels, unless accompanied by severe saturation, in which case the model would not be valid, as previously mentioned. Therefore, free-carrier and interconduction band absorption generally can be neglected in the intrinsic materials for which the bandgap energy is larger than the photon energy.

Waveguide Transfer Curve Model

In this section, the concept of absorption is generalized to include waveguide devices, and a relationship for the transfer curve of the EA waveguide modulator is developed. Two additional parameters from guided-wave theory are required to reconcile geometrical differences between absorption in a bulk of material and in the waveguide. The transfer curve model obtained is used to compare empirical absorption data to the absorption coefficients determined from theory.

Guided Wave Theory. Waveguiding in dielectric materials is caused by a central (core) region having a higher refractive index than the surrounding (cladding) layers. The guided mode field extends into the cladding layers with an evanescent (exponential) decay. Therefore, the core material does not contain all of the optical energy. Calculation of Poynting's vector from the field solutions of the wave equation give the average power distributed in each of the dielectric layers. The parameter Γ is the ratio of optical power in the waveguide core to the total power in the waveguide. Γ is sometimes called the optical confinement factor or optical filling factor, as it describes how much of the light is confined to (or fills) the core layer of the waveguide. The coupling efficiency to the optical fibers that transport the light into and out of the semiconductor waveguide is also of interest. In this discussion, the coupling efficiency per facet is referred to as C.

Both Γ and C are physical parameters related to the geometry of the waveguide structure and are determined by the wavelength of the light, thickness of the layers, and the relative dielectric constants of the layers. The schematic in Fig. 3 shows the cross-section of a stripe-loaded waveguide, which is a special form of asymmetric slab-coupled waveguide. The propagation characteristics are determined from the effective

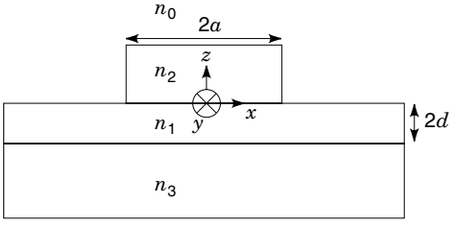

Figure 3. The schematic cross section of a stripe-loaded waveguide, with absorbing layer height $2d$ and stripe width $2a$. Light is confined primarily in region 1 under the stripe.

index method (33), in which the vertical and horizontal confinement are treated separately. Light confinement is achieved vertically (the z-direction) by using materials with

$$n_1 > n_2,\ n_3 > n_0 \tag{33}$$

where n_i refers to the refractive index of layer i. In the horizontal direction, confinement is achieved due to the waveguide under the stripe having a larger effective index than the portions of the waveguide not under the stripe. If the center section is imagined to be infinite in extent in the x-direction, the waveguide reduces to a four-layer slab waveguide. The two side sections become three-layer slab waveguides in the infinite approximation. Each of these sections is assigned an effective index from their respective solutions to the guided-mode eigenvalue equations. The horizontal confinement (in the x-direction) is determined from the solution of an effective slab waveguide in the vertical direction, using the effective indices of the three vertical problems. The solution to this slab waveguide results in an effective index for the whole structure, from which the electric fields are calculated.

Waveguide analysis shows the structure has both quasi-TE and quasi-TM mode solutions. The electric and magnetic fields are used in the calculation of both Γ and C. Poynting's theorem is used in both cases. This theorem states the electromagnetic wave power flow through a surface S is given by

$$W = \tfrac{1}{2} \oiint_S \boldsymbol{E} \times \boldsymbol{H}^* \cdot d\boldsymbol{A} \tag{34}$$

Only the y-component of the Poynting vector is selected, due to the dot product with the surface-normal area element. Therefore, the integral multiplies the transverse components of the fields. The y-component of the Poynting vector is proportional to $|E_x|^2$ for TE modes and $|H_x|^2/n_i^2$ for TM modes. Therefore the filling factors for each polarization are obtained according to

$$\Gamma_{\mathrm{TE}} = \frac{\displaystyle\int_{-a}^{a} dx \int_{-2d}^{0} dz \cdot |E_x|^2}{\displaystyle\int_{-\infty}^{\infty} dx \int_{-\infty}^{\infty} dz \cdot |E_x|^2} \tag{35a}$$

and

$$\Gamma_{\mathrm{TM}} = \frac{\dfrac{1}{n_1^2}\displaystyle\int_{-a}^{a} dx \int_{-2d}^{0} dz \cdot |H_x|^2}{\dfrac{1}{n_i^2}\displaystyle\int_{-\infty}^{\infty} dx \int_{-\infty}^{\infty} dz \cdot |H_x|^2} \tag{35b}$$

Due to the relationship $n_i^2 E_z \propto H_x$ for TM modes, the fact that $E_z \approx 0$ for TE modes, and that $E_x \approx 0$ for TM modes, one may rewrite Eq. (35) without loss of generality as

$$\Gamma = \frac{\displaystyle\int_{-a}^{a} dx \int_{-2d}^{0} dz \cdot |E_x^2 + E_z^2|}{\displaystyle\int_{-\infty}^{\infty} dx \int_{-\infty}^{\infty} dz \cdot |E_x^2 + E_z^2|} \tag{36}$$

for both TE and TM modes. The simulation space is actually a finite area chosen to be much larger than the stripe dimensions, and boundary conditions are imposed that require the fields to tend to zero at the boundaries. Thus the integration over all space reduces to the integration over the simulation area.

To calculate the coupling efficiency, the mode shape of the second waveguide must be specified. The coupling guides used in the experiments are glass lensed-fibers, made by machining a cone angle onto one end of standard single mode fiber. The circular symmetry of the fiber and the lens produce a Gaussian mode shape. The typical measured Gaussian spot size at the beam waist is 3 μm. Using a Gaussian field of the form

$$\boldsymbol{E}_1(\boldsymbol{r}) = \hat{e} E_1 e^{-(2r/w_0)^2} \tag{37}$$

where $\boldsymbol{r}$ is the position vector in the x–z plane with origin at the semiconductor waveguide mode maximum-field point and w_0 is the beam-waist spot size, the coupling efficiency is calculated

$$C = \frac{\left|\displaystyle\int_{-\infty}^{\infty} dx \int_{-\infty}^{\infty} dz \boldsymbol{E}_1 \cdot \boldsymbol{E}_2\right|^2}{\displaystyle\int_{-\infty}^{\infty} dx \int_{-\infty}^{\infty} dz |\boldsymbol{E}_1|^2 \times \int_{-\infty}^{\infty} dx \int_{-\infty}^{\infty} dz |\boldsymbol{E}_2|^2} \tag{38}$$

where $\boldsymbol{E}_2$ refers to the semiconductor waveguide mode field.

With the quantities Γ and C known, the expression for the absorbed power in Eq. (12) can be modified for the waveguide to

$$A(V) = P_{\mathrm{opt}} C (1 - R)(1 - e^{-\Gamma \alpha(V) L}) \tag{39}$$

accounting for the mode coupling efficiency and the distributed absorption due to a less-than-unity filling factor. The corresponding waveguide transmitted power is

$$T(V) = P_{\mathrm{opt}} C^2 (1 - R)^2 e^{-\Gamma \alpha(V) L} \tag{40}$$

where the second factor of $(1 - R)$ comes from the semiconductor to air interface at the waveguide output and the second factor of C for coupling to the output fiber. Using a weighted index value of 3.4 for the semiconductors, the Fresnel reflectance loss is 30% per facet. It is noted that the total Fresnel reflectance losses alone account for nearly 3 dB (50%) of the total loss in the transfer curve of the "as-cleaved" waveguide modulator. To reduce this loss, antireflection coatings are deposited onto the waveguide facets, which act as optical quarter-wave transformers to match the air and semiconductor indices.

The normalized transfer curve is often used for evaluating the voltage-dependent device performance. This normalized form is given by

$$T_N(V) = e^{-\Gamma \Delta\alpha(V) L} \tag{41}$$

where $\Delta\alpha(V) = \alpha(V) - \alpha(0)$. It is noted that Eq. (41) ignores the zero-bias residual loss from the built-in electric field. In such case, the residual absorption loss is grouped together with other bias-independent losses, such as those due to coupling efficiency and Fresnel reflection, to give a total device insertion loss.

Here it is also appropriate to comment on the interaction length. The length can be made long to accumulate a large change in transmission, even if the voltage-controlled change in absorption coefficient is small. However, this has two adverse effects on the device electrical performance. First, the longer length impacts the speed of the device, unless traveling-wave electrode design is used. In the case of the lumped element electrode, a longer length waveguide directly impacts the capacitance of the intrinsic device, approximated by the simple parallel plate capacitance relation

$$C_p = \frac{\epsilon w L}{d} \tag{42}$$

where w is the waveguide-stripe width and d is the intrinsic layer thickness. Second, the scattering and residual absorption loss coefficients of the waveguide are multiplied by the device length. To avoid excessively large optical insertion loss, care should be taken to make the device length short enough that still meets both speed and extinction requirements.

FKE Model Verification. Figure 4 shows typical measured transfer data at 1.318 μm wavelength for a 135 μm long FKE waveguide device. There is a distinct polarization anisotropy apparent in these curves. This is due primarily to the stronger absorption coefficient for the TM polarization, which results in the curve maximum slope occurring at a smaller dc bias than for the TE polarization. There are also slightly different optical overlaps between the optical modes and the electroabsorbing layer for the TE and TM polarizations in the waveguide.

For verification purposes one would like to use this measured data for a consistency check with the EA model. By taking the natural logarithm of the normalized transmission data and dividing by the device length and appropriate Γ factors, the change in absorption coefficient versus bias, $\Delta\alpha(V)$, is obtained. With the intrinsic-layer thickness fixed, there are two free-parameters in the model given by Eq. (10), the detuning energy, E_{det}, and the built-in voltage, V_{bi}. Appropriate values of E_{det} and V_{bi} are used to yield a continuous curve with

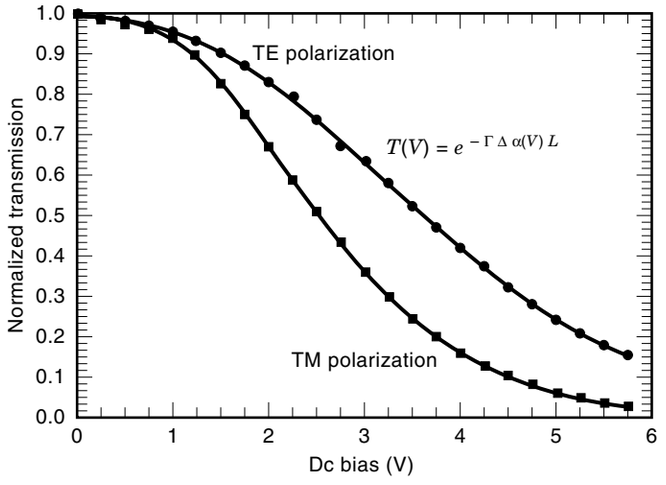

Figure 4. Measured transfer curves for a 135 μm-long FKE device at 1.318 μm in both polarizations, (circles: TE; squares: TM) showing the exponential dependence on bias.

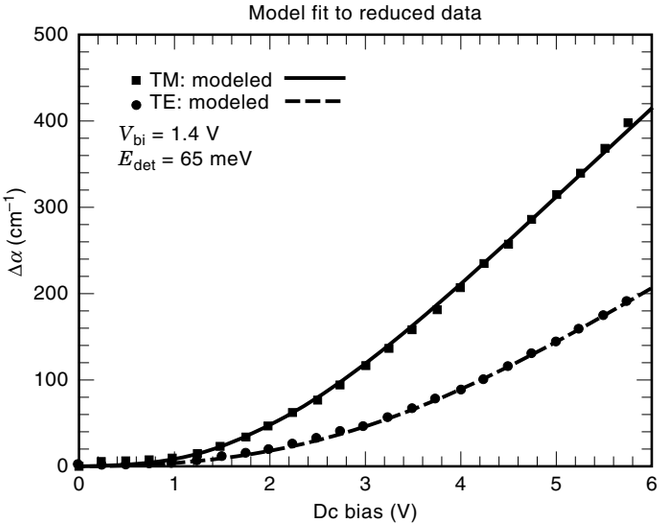

Figure 5. Change in FKE absorption coefficient versus bias for both the TE and TM polarizations. Data reduced from measured transfer curves (squares: TM; circles: TE) are used to model the absorption coefficient (TM: solid line, TE: dashed line) with appropriate values of V_{bi} and E_{det}.

the correct shape and curvature to fit the data of Fig. 4. This reduced transfer data versus bias is compared in Fig. 5 with the calculated absorption coefficients using Eq. (10). The detuning energy, E_{det}, is treated as a fit parameter to give the correct value of absorption at large applied bias. The figure shows good agreement between the measured and calculated $\Delta\alpha$ over the whole range of bias for both polarizations using a built-in voltage of 1.4 V and detuning energy of 65 meV. This detuning energy agrees quite well with the measured bandgap energy obtained using both photoluminescence (PL) and absorption spectroscopy. In the heterojunction diode, the p- and n-doping at the corresponding sides of the junction determine the built-in voltage. A built-in voltage of 1.4 V is calculated for the given structure using a finite element solver of the carrier transport equations. The close agreement between the model-fit parameters to the real diode V_{bi} and E_{det} validates the absorption coefficient model of Eq. (10).

The best measured optical insertion loss for the waveguide that produced the transfer curves of Fig. 4 is 8.8 dB for the TE polarization and 9.1 dB for the TM polarization. Substituting the V_{bi} fit-parameter into the absorption coefficient model, an estimate for the zero-bias insertion loss due to residual absorption along the waveguide core is obtained. For the TM polarization, residual absorption loss in the core is calculated to be 0.2 dB, and mode mismatch accounts for 7.2 dB loss. Fresnel losses are assumed negligible because of the anti-reflection coatings, so all other losses are estimated to be 1.7 dB. Other losses that contribute to the total fiber-to-fiber insertion loss are free-carrier absorption outside the absorbing layer, scattering loss from rough interfaces and the etched-rib sidewalls, and fiber scattering loss.

QCSE Model Verification. In order to assess the quantum well absorption model, surface-normal, spectral EA measurements are performed on ring diodes. Light is incident on the material normal to the surface rather than in a waveguide

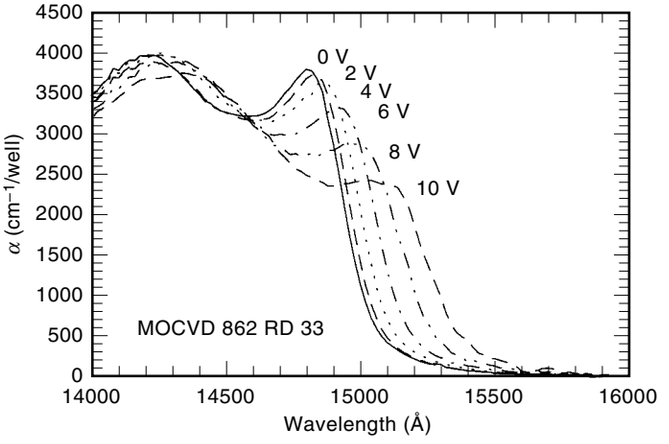

Figure 6. The absolute absorption spectra at 0, 2, 4, 6, 8, and 10 V measured from a sample consisting of a 25 period InGaAs/InP MQW, with well and barrier widths nominally grown 68 Å and 140 Å, respectively. The shift in the exciton peak to longer wavelength is evidence of the quantum-confined Stark effect.

configuration, which guarantees a TE polarization. Also, the optical confinement and coupling efficiency factors are both unity, facilitating a direct comparison of the modeled and measured $\alpha(\omega, V)$.

Absolute absorption spectra are obtained using both photocurrent and transmission measurement according to the method of Ref. 34. Light from a Tungsten white light source is passed through a monochromator, mechanical chopper, and focusing optics to the ring diode. More focusing optics and a Germanium photodetector are placed behind the diode. The signal from either the ring diode or the Ge diode is fed to a lock-in amplifier referenced to the chopper frequency. Transmission and photocurrent data is collected from the lock-in by a computer that also controls the sweep of the monochromator. A variable dc power supply biases the diode under test. Figure 6 shows the absolute absorption spectra measured from a sample consisting of a 25 period InGaAs/InP MQW, with well and barrier widths nominally grown 68 Å and 140 Å, respectively.

These spectra exhibit the three classic behaviors of the QCSE under an applied voltage. First, the exciton absorption peak shifts toward longer wavelengths. The energy shift is approximately 25 meV between the 0 V and 10 V curves. Second, there is a reduction in the oscillator strength, that is, the magnitude of the exciton peak diminishes with increasing bias. This follows as a consequence of the increased separation of electrons and holes and the reduced overlap in wavefunctions with applied field. Third, the linewidth of the peak broadens. In Fig. 6, the linewidth broadening is quite significant, suggesting additional broadening phenomenon such as interface roughness, well width variation, or nonuniform field distribution in the different wells due to large background doping.

The experimental data of Fig. 6 are used to verify the QCSE model. The measured zero-bias exciton has a Gaussian lineshape with a FWHM of 12.8 meV, which is used as an input parameter to the model. The correct Stark shifts and exciton peak energy positions are obtained for a 53 Å well and 1.0 V built-in voltage for the 0.52 μm thick intrinsic layer. The well width expected from calibrated growth rates is 68 Å. The 15 Å discrepancy in well width is actually not a failure of the absorption model, but can be explained as follows: X-ray diffraction analysis on these quantum well materials indicates that As carryover and As-P substitution across the InP-on-InGaAs interface is occurring for this material. The complex dynamics of the As exchange and transport create an interfacial layer of strained InAsP material which depletes part of the InGaAs well. Reference 35 has measured a 0.26% vertical strain (compressive in the plane of the layers) for a 20 period InGaAs/InP MQW, grown under similar conditions to the material that produced the spectra of Fig. 6. The strain analysis suggests an InAsP layer thickness per period of at least 10 Å to 36 Å in extent, which reduces the InGaAs well thickness, consistent with the QCSE model-fit. Cross-sectional scanning-tunneling microscopy (STM) has also been

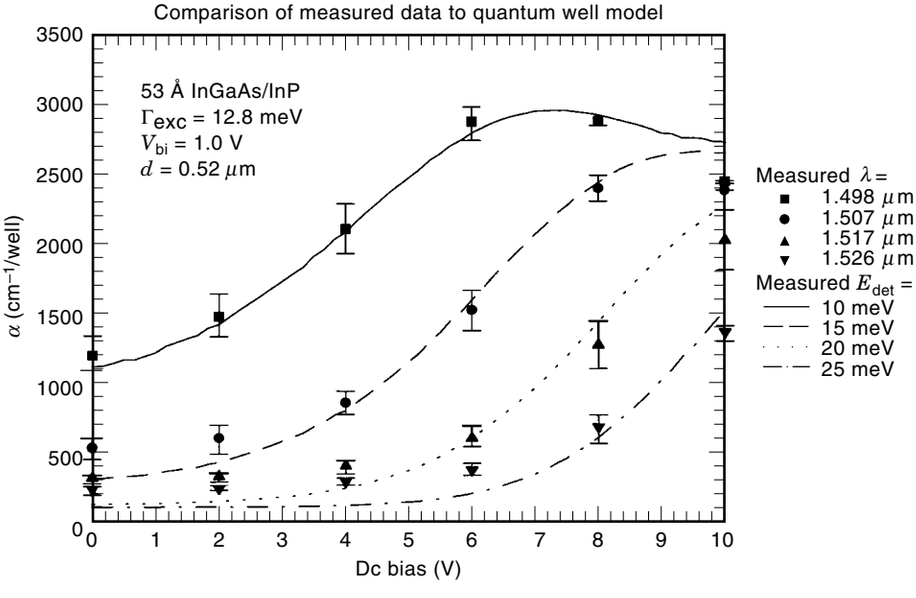

Figure 7. Comparison of the absolute absorption values of the QCSE model and the experimental data at four fixed optical wavelengths. The QCSE model uses a zero-bias exciton Gaussian lineshape (FWHM of 12.8 meV), a 53 Å well width, and a 1.0 V built-in voltage over the 0.52 μm intrinsic layer, producing the correct Stark shifts and exciton peak energy positions to match the measured data.

done on this material, which verifies the smaller well width, an extended interfacial layer of intermediate bandgap, and well width inhomogeneity (36).

Comparison of the absolute absorption values for the QCSE model and the experimental data at four fixed optical wavelengths is shown in Fig. 7. As seen in the figure, there is very good agreement between the model and the measured data for values of the absorption coefficient greater than 500 cm^{-1}, but very poor agreement for values less than 500 cm^{-1}. This may be due to a very large degree of interfacial scattering in the quantum well. The large sensitivity in the absorption coefficient to the detuning energy is also noted. The error bars in Fig. 7 represent approximately ± 1 meV variations in the detuning energy, the resolution of the measurement. For the modeled absorption coefficients, the difference in detuning energies between adjacent curves is only 5 meV. Thus, a 5 meV change in detuning energy could result in a change in absorption in excess of 1000 cm^{-1}.

CONCLUSION

In conclusion, a simple exponential expression is used to model the electroabsorption characteristics of bulk and quantum well semiconductor materials. These models can be used to predict the performance of electroabsorption modulators in fiber optic links. Lumped-element electroabsorption waveguide modulators show superior performance in bandwidth-voltage ratio to impedance- and velocity-matched Mach–Zehnder modulators. As components for optical communication links, EA modulators can meet high-speed and low-drive voltage requirements.

BIBLIOGRAPHY

1. D. F. Blossey and P. Handler, Electroabsorption, in R. K. Willardson and A. C. Beer (eds.), *Semiconductors and Semimetals: Modulation Techniques,* New York: Academic Press, 1972.
2. T. R. Chung et al., 1.3 μm InGaAsP/InP lasers on GaAs substrate fabricated by the surface activated wafer bonding method at room temperature, *Appl. Phys. Lett.,* **72** (13): 1565–1566, 1998.
3. S. Schmitt-Rink et al., How fast is excitonic electroabsorption? *Opt. Lett.,* **15** (1): 60–62, 1990.
4. N. K. Dutta et al., Frequency chirp under current modulation in InGaAsP injection lasers, *J. Appl. Phys.,* **56** (7): 2167–2169, 1984.
5. J. A. J. Fells et al., Transmission beyond the dispersion limit using a negative chirp electroabsorption modulator, *Electron. Lett.,* **30** (14): 1168–1169, 1994.
6. R. C. Alferness, Waveguide electrooptic modulators, *IEEE Trans. Microw. Theory Tech.,* **MTT-30**: 1121–1137, 1982.
7. K. Noguchi, H. Miyazawa, and O. Mitomi, 75-GHz Ti:$LiNbO_3$ Optical Modulator, in *Optical Fiber Commun., 1994 OSA Tech. Dig. Series* (Optical Society of America, Washington, DC), paper WB3, 1994, vol. 4, pp. 76–77.
8. W. Franz, Einfluβ eines elektrischen Feldes auf eine optische Absorptionskante, *Z. Naturforschg.,* **13a**: 484–489, 1958.
9. L. V. Keldysh, *Zh. Eksperim i. Teor. Fiz.,* **34**: 1138–1141, 1958 (English translation: The effect of a strong electric field on the optical properties of insulating crystals, *Sov. Phys.-JETP,* **7** (5): 788–790, 1958).
10. D. A. B. Miller et al., Band-edge electroabsorption in quantum well structures: The quantum-confined Stark effects, *Phys. Rev. Lett.,* **53** (22): 2173–2176, 1984.
11. R. Dingle, W. Wiegmann, and C. H. Henry, Quantum states of confined carriers in very thin $Al_xGa_{1-x}As/GaAs/Al_xGa_{1-x}As$ heterostructures, *Phys. Rev. Lett.,* **33** (14): 827–830, 1974.
12. G. H. Wannier, The structure of electronic excitation levels in insulating crystals, *Phys. Rev.,* **52**: 191–197, 1937.
13. T. Ido, S. Tanaka, and H. Inoue, MQW electroabsorption modulators for 40 Gbit/s TDM systems, in *Optical Fiber Commun., 1997 OSA Tech. Dig. Series* (Optical Society of America, Washington, D.C.), vol. 6, paper WG5, 1997, pp. 140–141.
14. S. Oshiba, K. Nakamra, and H. Horikawa, High-efficiency electroabsorption modulator to generate 20 GHz-3.6 ps transform-limited optical pulses, in *Optical Fiber Commun., 1997 OSA Tech. Dig. Series* (Optical Society of America, Washington, D.C.), vol. 6, paper WG2, 1997, pp. 136–137.
15. G. Mak et al., High-speed bulk InGaAsP-InP electroabsorption modulators with bandwidth in excess of 20 GHz, *IEEE Photon. Technol. Lett.,* **2** (10): 730–733, 1990.
16. T. H. Wood et al., Electric field screening by photogenerated holes in MQWs: A new mechanism for absorption saturation, *Appl. Phys. Lett.,* **57**: 1081–1083, 1990.
17. I. K. Czajkowski et al., Strain-compensated MQW electroabsorption modulator for increased optical power handling, *Electron. Lett.,* **30** (11): 900–901, 1994.
18. F. Devaux et al., InGaAsP/InGaAsP/InAsP MQW polarization-independent modulator with high optical power saturation, in *Optical Fiber Commun., 1997 OSA Tech. Dig. Series* (Optical Society of America, Washington, D.C.), vol. 6, paper WG4, 1997, pp. 139–140.
19. G. Dresselhaus, Effective mass approximation for excitons, *J. Phys. Chem. Solids,* **1**: 14–22, 1956.
20. D. E. Aspnes and N. Bottka, Electric-field effects on the dielectric function of semiconductors and insulators, in R. K. Willardson and A. C. Beer (eds.), *Semiconductors and Semimetal: Modulation Techniques,* New York: Academic Press, 1972.
21. D. E. Aspnes, Electric field effects on the dielectric constant of solids, *Phys. Rev.,* **153** (3): 972–982, 1967.
22. S. Gasiorowicz, *Quantum Physics,* New York: Wiley, 1974.
23. R. J. Elliot, Intensity of optical absorption by excitons, *Phys. Rev.,* **108** (6): 1384–1389, 1957.
24. K. Tharmalingam, Optical absorption in the presence of a uniform field, *Phys. Rev.,* **130** (6): 2204–2206, 1963.
25. D. A. B. Miller et al., Electric field dependence of optical absorption near the band gap of quantum-well structures, *Phys. Rev. B,* **32** (2): 1043–1060, 1985.
26. A. I. Anselm, *Introduction to Semiconductor Theory,* Englewood Cliffs, NJ: Prentice-Hall, 1981, pp. 447–455.
27. D. S. Chemla and D. A. B. Miller, Room-temperature excitonic nonlinear-optical effects in semiconductor quantum-well structures, *J. Opt. Soc. Am. B,* **2** (7): 1155–1173, 1985.
28. J. M. Luttinger and W. Kohn, Motion of electrons and holes in perturbed periodic fields, *Phys. Rev.,* **97** (4): 869–883, 1955.
29. P. Lawaetz, Valence-band parameters in cubic semiconductors, *Phys. Rev. B,* **4** (10): 3460–3467, 1971.
30. D. A. B. Miller, J. S. Weiner, and D. S. Chemla, Electric-field dependence of linear optical properties in quantum well structures: Waveguide electroabsorption and sum rules, *IEEE J. Quantum Electron.,* **QE-22** (9): 1816–1830, 1986.
31. K. J. Williams, R. D. Esman, and M. Dagenais, Nonlinearities in p-i-n microwave photodetectors, *IEEE J. Lightwave Technol.,* **14** (1): 84–96, 1996.
32. H. C. Huang, S. Yee, and M. Soma, The carrier effects on the change of refractive index for n-type GaAs at λ = 1.06, 1.3, and 1.55 μm, *J. Appl. Phys.,* **67** (3): 1497–1503, 1990.

33. R. M. Knox and P. P. Toulios, Integrated circuits for the millimeter through optical frequency range, in *Symp. Submillimeter Waves, Proc. MRI,* New York: Polytechnic Press, 1970, p. 497.

34. A. N. Cheng, *Quaternary InGaAlAs/InAlAs quantum wells for 1.3 μm electro-absorption modulators,* Ph.D. dissertation, Univ. California, San Diego, Chapters 3, 4, 1994.

35. X. S. Jiang, A. R. Clawson, and P. K. L. Yu, Study of interrupted MOVPE growth of InGaAs/InP superlattice, *J. Crystal Growth,* **124** (4): 547–552, 1992.

36. A. Y. Lew et al., Interface structure in Arsenide/Phosphide heterostructures grown by gas-source MBE and low-pressure MOVPE, *J. Electron. Mater.,* **26** (2): 64–69, 1997.

ROBERT B. WELSTAND
Applied Micro Circuit Corporation

STEPHEN A. PAPPERT
SPAWAR System Center

PAUL K. L. YU
University of California, San Diego

ELECTRO-ACOUSTICAL ANALOGIES. See ACOUSTIC VARIABLES MEASUREMENT.